Photonic Quantum-Inspired Sub-Diffraction Imager for Space Debris Characterization

Stephen S. Eikenberry[a,b], Rodrigo Amezcua-Correa[a], Kerri Donaldson-Hanna[b], Robert Conwell[a], Matthew Cooper[a] Tara Crowe[a], Caleb Dobias[a], Christina Moraitis[a,b], Miguel Romer[a]

[a]College of Optics and Photonics (CREOL), University of Central Florida

[b]Department of Physics, University of Central Florida

ABSTRACT

We present our project to develop, test, and demonstrate a Photonic Quantum Inspired Imager (PQI2) in response to the AFRL Grand Challenge on quantum inspired (QI) space debris imaging below the diffraction limit. Space debris presents a serious threat to the future of space research and commercialization for the United States and the world at large. A crucial first step towards mitigating the threat posed by space debris is extreme resolution imaging to reveal the nature of space debris — including, the size, shape, composition, rotation, and time evolution of individual objects. A major constraint for implementing leading QI concepts is that they require a device to perform spatial mode multiplexing in an efficient and accurate manner. Our group has demonstrated exactly such a photonic spatial mode sorter quantum-sensing device in practice — a photonic lantern — with capabilities in both spatial and spectral diversity, as well as future extensions to polarization sensitivity. Over the past 5 years, our group has developed high-efficiency photonic lantern mode-sorting/multiplexing devices fabricated in optical fibers. Our proposed passive imaging system is therefore based on three main innovations: (i) photonic lantern spatial mode sorters with spatial and spectral diversity, (ii) atmospheric blur removal enabled by mode-/wavelength-resolution, (iii) astronomy-inspired machine learning image reconstruction techniques. We present the current status of design and component-level testing of PQI2.

Keywords: Imaging; quantum-inspired imaging; hyperspectral imaging; atmospheric turbulence; photonic lantern; astrophotonics; space debris, space domain awareness

1. INTRODUCTION

Space debris presents a serious threat to future space research and commercialization for the United States and the world at large. Space debris has been an increasing problem since the launch of the first artificial satellite in 1957 marking the beginning of the space age. The potentially catastrophic effects of "space junk" are being voiced not only by NASA, but the Space Force, the entire commercial space industry, and the US President. Current studies estimate 100 million pieces of space debris in orbit — many too small to track with current imaging technology. Debris as small as a marble traveling at an orbital velocity of 17,500 mph can cause mission-ending damage to spacecraft and satellites. This could potentially destroy capabilities to monitor hurricanes, distribute GPS navigation signals, and provide critical communication links to tactical personnel protecting US national security in hazardous areas across the globe. Due to the potential damage from such small objects, the White House has published a National Orbital Debris Implementation Plan (2021-2022), emphasizing the need to limit the debris created during space operations, and pushing for improved capabilities in tracking, characterizing, and even removing the space debris. It is standard operating procedure to monitor the space domain within a large area near spacecraft such that operators have enough time to enact evasive maneuvers if debris crosses into the designated area. The International Space Station requires a $2.5\times30\times30$ mile imaginary box for this reason. China and Russia have both intentionally destroyed objects in space within the past few years. China was showcasing their abilities for anti-satellite operations, and Russia destroyed their own defunct satellite, throwing up a significant amount of additional space debris and interfering with national security. Unfortunately, it is common practice for space assets to be destroyed intentionally by their operators once the operational life of the asset is finished. Additionally, advances in space

technology and operations bring new risks of active and passive space-to-space operations against spacecraft/satellites under the guise of space debris.

A crucial first step towards mitigating the threat posed by space debris is improved information on the nature of space debris objects, including, the size, shape, composition, rotation, and time evolution of individual objects. Imaging angular resolution poses a significant challenge for measuring these properties due to the key limiting factors of diffraction and atmospheric turbulence. Atmospheric turbulence degrades image resolution by perturbing the phase of an incident wavefront propagating through the varying density (and thus optical refractive index) of turbulent cells. These cells create a Kolmogorov power spectrum of phase variations which change on timescales of ~100 to 1000 Hz, depending on the prevalent atmospheric conditions and wind speeds. The typical optical coherence length of the atmosphere, the Fried parameter r0, ranges from a few cm to 10+ cm in the visible band and produces time-averaged profiles resembling Gaussian Point Spread Functions (PSFs) with typical sizes of $\sim\lambda/r0$ full width at half maximum (FWHM). Uncorrected, these atmospheric effects would limit study of space debris objects to size scales >1-meter at Low Earth Orbit (LEO) and >100-meters at Geostationary Orbit (GEO). A high-cost solution to this longstanding problem developed over the last few decades uses an adaptive optics system to first sense the wavefront aberrations produced by the atmosphere, and then correct them with a deformable mirror optically conjugated to one or more turbulent layers in the atmosphere. Such systems generally require a reference light source (either a natural or laser-generated guide star) to provide sufficient light to measure the aberrations at the ~1-10 ms coherence timescales of the atmosphere. Most AO systems to-date work at near-infrared wavelengths, where the larger atmospheric Fried parameter makes wavefront correction more tractable. These systems can produce images at the diffraction limit (DL) of the telescopes, with PSFs at FWHM $\sim\lambda/D$. For a 3.67-m telescope such as the AEOS facility on Maui, this results in the ability to resolve debris objects down to ~10cm in Low Earth Orbit (LEO) and down to ~10m in geostationary (GEO) orbits. Unfortunately, **this still falls short of the ~1cm resolution needed to address this problem.**

2. PHOTONIC QUANTUM-INSPIRED IMAGER (PQI2)

Breakthrough imaging concepts capable of overcoming the DL require innovative components to spatially decompose the collected light in parallel with advanced image correction and reconstruction algorithms [1, and references therein]. Over the past 5 years, our group has developed high-efficiency photonic lantern mode-sorting/multiplexing devices fabricated in optical fibers [2,3]. This enables a new paradigm for "all-fiber" photonic lantern mode sorters [4,5,6,7] for sub-DL imaging applications. Our approach borrows heavily from multimode beam processing techniques recently demonstrated in high-resolution astronomical instrumentation and in ultra-high capacity optical communication systems. Unlike bulk optic mode-sorting schemes, our photonic lantern mode multiplexers offer extremely high efficiencies and operate over large bandwidths - all without additional mechanisms to actively maintain alignment or specially-designed thermally-stabilized passive mounts. Thus, our proposed PQI2 system, shown in Fig.1, is based on three main innovations: (i) photonic lantern spatial mode sorters with spatial and spectral diversity, (ii) atmospheric blur removal enabled by mode/wavelength resolution, (iii) transfer matrix and machine learning QI image reconstruction techniques.

Having introduced our technical approach, we will now discuss the specific technology requirements related to space debris imaging. Debris objects in orbit produce a wavelength-dependent source function due to solar illumination which we aim to reproduce from observational data. However, for debris separations or structure on scales smaller than the telescope DL, the image will have overlapping PSFs. Furthermore, for ground-based observations as envisioned here, the atmosphere produces strong phase variations which degrade the PSF by a factor of >30 typically at visible wavelengths, and which change on timescales of ~1-10 ms (100-1000 Hz). Thus, we are initially at a factor of ~100 away from the necessary resolution, with rapidly evolving aberrations – a problem previously considered to be intractable. However, innovations in techniques and photonic lantern hardware enable new solutions to this problem which can in fact approach the quantum resolution limit via mode-demultiplexing sensors.

The difficulty of implementing the mode demultiplexing technologies required for sub-DL space debris imaging arises from the highly multimode nature of the light being collected by the telescope. This demands high efficiency mode sorting devices supporting ~1000 spatial modes with outputs that can be easily interfaced to single-mode fibers. Our solution to this problem, relies on photonic lanterns which combine wave intensity and phase shifts in the spatial dimension to achieve such mode sorting. They consist of a smooth continuous 3-D waveguide transition which implements spatial transformations. The photonic lantern mode multiplexer thus accepts a multimode wavefront/image and converts it into an array of spatially separated single mode beams at high (>90%) optical efficiency. The lantern performs mode mapping equivalent to a transfer matrix operation from the multimode fiber modal basis to a basis consisting of an array of Gaussian

beams. This transformation projects the phase/amplitude morphology of the incident light onto a linear combination of modes at the multimode input of the lantern. These in turn map to unique intensity patterns at the single-mode fiber outputs. Thus, we can measure the distribution of intensities among the output single mode beams to reconstruct the incoming optical field via QI image retrieval algorithms. We fabricate our photonic lanterns by fusing and tapering different fibers and glass capillaries together in our state-of-the-art Fiber Microdevice Facility at CREOL, producing lanterns that move from a multimode fiber input to an output array of isolated single-mode fibers. The all-fiber construction allows us to build mode multiplexers engaging >1000s of modes with losses <1 dB over blue to near-infrared wavelengths simultaneously.
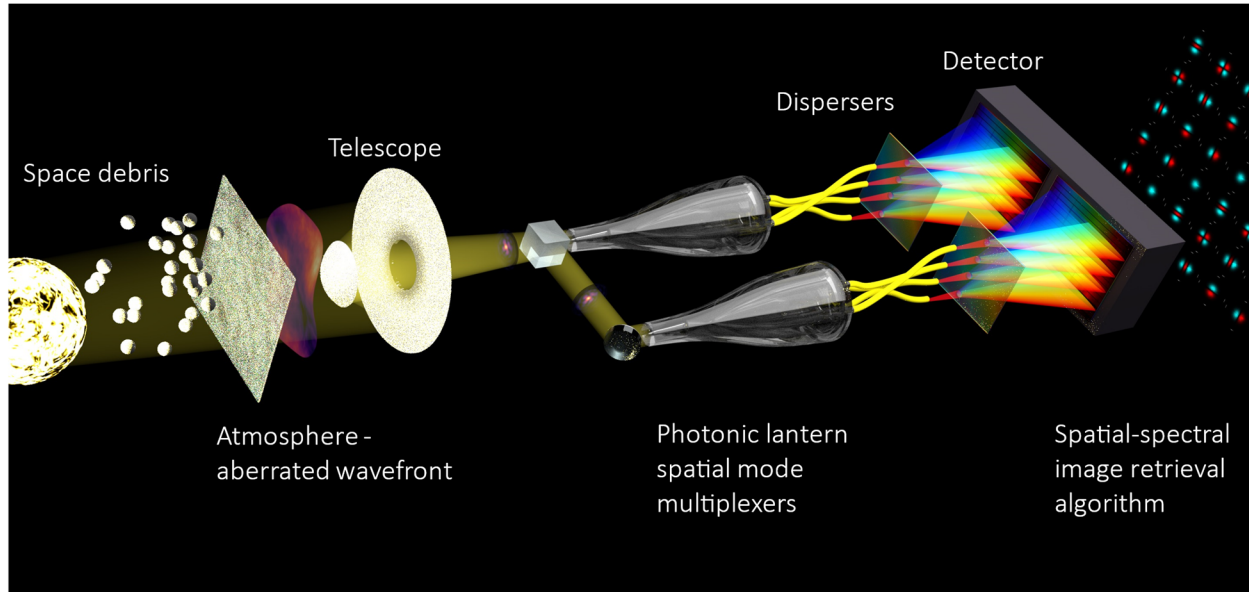

*Fig 1 - **Photonic Quantum Inspired Imager Concept**. A telescope points to and tracks the debris target, simultaneously imaged through a system of two photonic lantern spatial mode sorters in broadband light. The photonic lanterns are judiciously designed to map the collected image into two distinct modal bases. This allows us to fully reconstruct the incoming optical field unambiguously (amplitude and phase) via an inverse mapping algorithm. Each photonic lantern outputs the light through single mode fibers with their ends arranged in a square array. The light then passes through a standard low-resolution ($R = \lambda/\mathrm{\Delta\lambda} = 200$) spectrograph with a collimator, dispersing prism, camera, and high-speed CMOS detector. This produces an array of separated mode spectra on the detector. We then read out the modal spectra at frame rates of ~500 Hz (up to 1 kHz, as needed), combining this information to provide the full modal phase and intensity versus wavelength as described above, reconstructing the image with resolution approaching the Cramer-Rao Lower Bound quantum limit.*

To remove time-dependent atmospheric blur, our approach eschews adaptive optics, and instead uses the intrinsic spectral diversity of the limiting resolution factors (λ/D for diffraction, $\sim\lambda/r_0$ for atmospheric turbulence) to break the degeneracy between these aberrating processes. Specifically, the Fried parameter r_0 scales as $\lambda^{6/5}$, so the atmospheric turbulence resolution changes only weakly with wavelength as $\lambda^{-1/5}$ (and with the opposite trend of the DL, λ^1). This fact has been commonly exploited by astronomy for decades to achieve diffraction limited imaging. Similarly, we can use the spectral diversity provided by our passive photonic lantern mode multiplexer to first solve for the atmospheric phase variations (near-constant in λ, but rapidly varying in time) to effectively "freeze" the residual modal information due to the source function and diffraction. This allows implementation of QI image retrieval algorithms linked to machine learning code to reconstruct the sub-DL image. Importantly, we achieve this without splitting the light between "sensing" and "science" channels, so that all the light is available for imaging.

We have simulated the performance of such a system as shown in Fig 2. We show a simple sub-DL object source function comprised of two small (modeled as point-like) pieces separated by 5cm at an altitude of 300 km separated by ~0.5x the Rayleigh criterion on a 3.7-m telescope at visible wavelength and illuminated by the Sun with 30% albedo (broadband averaged). We assume that one object is an asteroid fragment with a Juno-like spectrum, while the other has a modified solar spectrum expected from artificial satellite albedo. We then calculate the observed light distribution with diffraction included. Next, we add time-variable phase aberrations introduced at the telescope pupil by atmospheric turbulence with

a Kolmogorov power spectrum and r_0=10cm to produce a simulated observed light distribution at the telescope. We then simulate the full modal measurement versus wavelength provided by our passive spatial/spectral mode demultiplexing photonic lantern devices described above. We then simulate the spectral detector illumination and noise and apply the reconstruction techniques described, leading to a simulated recovered source function as a function of wavelength. The resulting image meets the AFRL Grand Challenge in the imaging space. At the same time, we also capture the intrinsic spectral diversity in the targets, distinguishing natural from artificial sources in LEO/GEO. This will serve as a transformative technology granting us new capabilities spanning across multiple sensing domains, enabling us to meet the critical needs of debris imaging and characterization.

These simulations highlight some key strengths of our approach. The intrinsic spectral diversity provided by our spatial/spectral mode demultiplexing photonic lanterns naturally separates non-degeneracies in the source function of targets, providing important insights into composition/structural differences. This stands in strong contrast to broadband or bandpass devices which suffer from spectral confusion of general unknown source spectral features and/or limited spectral throughput and sensitivity. Our approach can also be upgraded to employ 4 of the photonic lantern sensors together with polarization-analyzing bulk optics to provide linear polarization measurements with improved sensitivity for target structures with polarization diversity. Such polarization features should be commonly encountered for sub-DL space debris due to scattering-induced polarization of the incoming sunlight off the differing shapes/orientations of the sub-structure components.
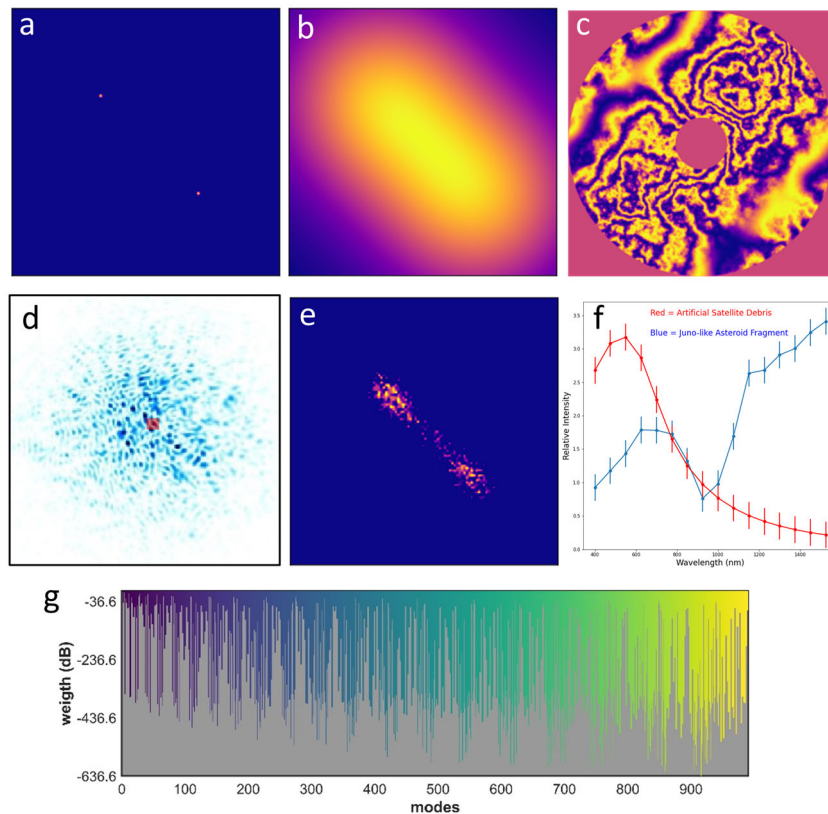

Fig 2 - **Simulated Image collection and reconstruction.** (a) Source distribution function (wavelength-stacked) with 5cm separation at LEO. (b) DL light distribution from a 3.7-m telescope. (c) Simulated snapshot in time of atmospheric phase aberrations at the telescope pupil with $r_0 = 10$cm. (d) Simulated observed light distribution including atmospheric turbulence. Inset square shows the size of the source function and DL images. (e) Simulated recovered source function image (wavelength-stacked) after simulating detector response/noise and applying quantum-inspired image recovery algorithms. (f) Simulated spectral intensity of the two diverse objects. (g) Modal decomposition derived from (d), used for steps e-f.

3. PQI2 SIMULATION FRAMEWORK

We base our simulations of the PQI2 system performance on the design concept and related data analyses planned for the actual measurements. We begin by introducing a mathematical framework, beginning with the following definitions:

S = source function over (x, y, λ)

P = complex Point Spread Function (PSF) over (x, y, λ)

D = diffraction-limited complex image = $P * S$ (the convolution of the source function with the PSF)

A = atmospheric turbulence phase function

R = received image at entrance of Photonic Lantern = $A(P * S)$

T = transfer function of Photonic Lantern (input modes to output modes)

M = measured modal signals (amplitude and phase) $= TR = TA(P * S)$

Given the measured modal signal and the lab-calibrated transfer function, we can see that the (complex-valued) received image is

$$R = T^{-1}M \text{ (Eqn 1)}$$

A, Photonic Lantern Transfer Matrix

In order to move from the measured modal amplitudes and phases (M) to the received image (R), we require a simulated transfer matrix (T). The non-mode-selective photonic lanterns we consider here effectively provide randomly-scrambled modal transfer functions. Thus, we represent each lantern transfer matrix as a random unitary matrix. We then create a distribution of input conditions (complex vectors matching number of modes), and apply an extended version of the Gerberch-Saxton algorithm to determine the phases from the measured intensities at the output ports of the photonic lantern. This iterative algorithm operates on the input data until it converges to a solution within an acceptable tolerance on the phase-amplitude vector. Once this solution convereges, we have both *T* and *M*, and thus can determine *R* – the received image at the entrance of the photonic lantern. We present results from these simulations in section IV.A below.

B. Turbulence Phase Retrieval

Following from our initial equations, $R = \text{FFT}[Pupil \times e^{-i\phi} \times FFT(S)]$ where $\phi(a, b, t, \lambda)$ is the turbulent phase deviation as a function of position on the pupil, time, and wavelength. The Pupil is also defined over (a, b).

$$R' \equiv \text{FFT}^{-1}(R) = \text{Pupil} \times e^{-i\phi} \times \text{FFT}(S) \text{ (Eqn 1)}$$

$$S' \equiv \text{FFT}(S)$$

$$\ln(R') = \ln(\text{Pupil}) - i\phi + \ln(S') \text{ (Eqn 3)}$$

Now, the Pupil mask is an array that is either 1 or 0. So, for the Pupil=0 pixels, this equation is undefined. However, we do not care about those pixels, since they are not illuminated. For pixels with Pupil(a,b) = 1, we then have:

$$\ln(R') = -i\phi + \ln(S') \text{ (Eqn 4)}$$

Solving for phase, we have

$$\phi = i[\ln(R') - \ln(S')] \text{ (Eqn 5)}$$

We now consider two wavelengths and the phase functions there, $\phi_{(a,b,t,\lambda)}$. This gives a phase difference

$$\phi_{\lambda_1} - \phi_{\lambda_2} = i\left[\ln R'_{\lambda_1} - \ln R'_{\lambda_2}\right] - i\left[\ln S'_{\lambda_1} - \ln S'_{\lambda_2}\right]$$

Assuming that the source function is constant (or nearly constant) across this wavelength difference, we have

$$\phi_{\lambda_1} - \phi_{\lambda_2} = i\left[\ln R'_{\lambda_1} - \ln R'_{\lambda_2}\right] \text{ (Eqn 6)}$$

Now, the atmospheric turbulence phase distribution follows the functional form:

$$\phi_\lambda = (n_\lambda - 1)\,\phi_0 \text{ (Eqn 7)}$$

where n_λ is the (known) index of refraction at that wavelength. The parameter ϕ_0 is the structure of the phase function – equivalent to the differential Optical Path Length (OPL) through the atmosphere. With ϕ_0, we can calculate the turbulent phase at any wavelength. Combining equations 6 and 7 gives

$$\phi_0\big[n_{\lambda_1} - 1 - n_{\lambda_2} - 1\big] = i\big[\ln R'_{\lambda_1} - \ln R'_{\lambda_2}\big] = i\ln\frac{R'_{\lambda_1}}{R'_{\lambda_2}}$$

$$\phi_0\big[n_{\lambda_1} - n_{\lambda_2}\big] = i\ln\frac{R'_{\lambda_1}}{R'_{\lambda_2}}$$

$$\phi_0 = \frac{i}{n_{\lambda_1} - n_{\lambda_2}}\ln\frac{R'_{\lambda_1}}{R'_{\lambda_2}}$$

So, if we have two measured response functions at two known wavelengths, we can determine the underlaying phase distribution parameter, and then calculate phase at any wavelength.

For N different wavelength bins and a given reference wavelength λ selected from them, the average estimator for the phase parameter is

$$\widehat{\phi}_0(\lambda) = \frac{1}{N}\sum_\gamma \frac{i}{n_\lambda - n_\gamma}\ln\frac{R'_\lambda}{R'_\gamma}$$

$$\widehat{\phi}_0(\lambda) = \frac{1}{N}\sum_\gamma \frac{i}{n_\lambda - n_\gamma}\big[\ln R'_\lambda - \ln R'_\gamma\big]$$

Then, we can find the overall optimal estimator

$$\widehat{\phi}_0 = \frac{i}{N^2}\sum_\lambda\sum_\gamma \frac{1}{n_\lambda - n_\gamma}\big[\ln R'_\lambda - \ln R'_\gamma\big]$$

This is for a given time slice, and over all pupil plane pixels. The outcome of this process is then a phase distribution over the pupil as a function of wavelength for a given time slice.

C. Sub-Diffraction Source Function Reconstruction

Several approaches exist for reconstructing a sub-diffraction source function from a measured light distribution containing the phase and amplitude information of the electric field. We developed a simple sub-DL-optimized approach. We calculate complex PSFs on a finely-sampled sub-diffraction grid. We then calculate the best-fit intensity distribution over these PSFs with respect to the measured response (*R* above). We present an example in Fig 3. This approach works well for source functions down to separations of ~0.1 λ/D and below. We describe this further below.
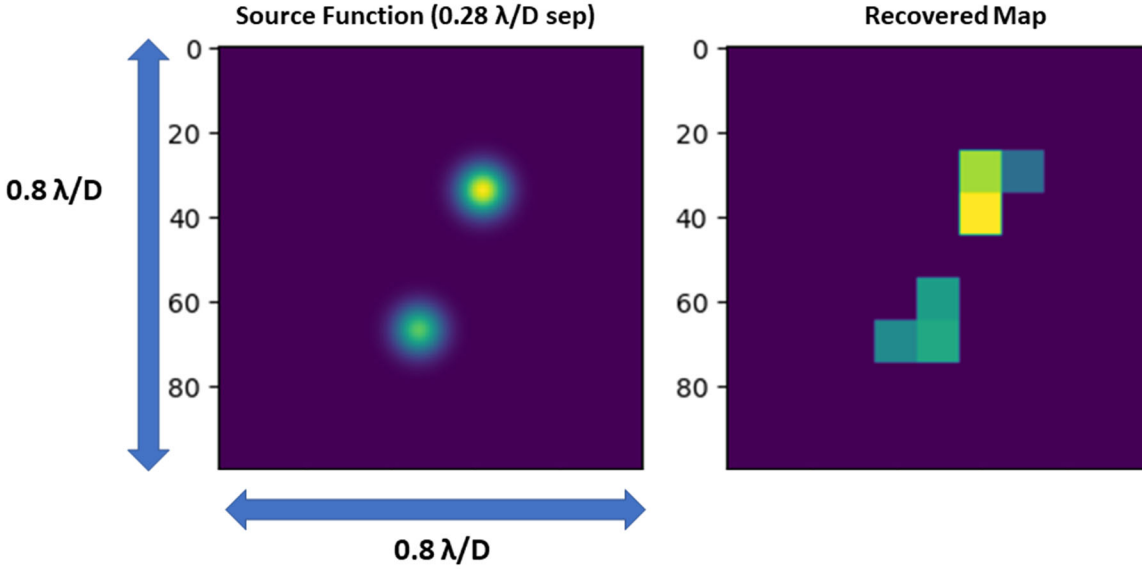
Fig 3 *– (Left) Input 2-source function with separation of 0.28 λ/D. (Right) Reconstructed map of the source function extracted from a complex image (similar to those seen in Fig 2). Note that the location, separation, and relative brightnesses of the sources is recovered in this map.*

4. PRELIMINARY SIMULATION RESULTS

A. Transfer Matrix

We used the simulation framework to explore the ability to reconstruct phase and amplitude for N modes based on intensity measurements alone. We note that the number of degrees of freedom is *2N*, but *2N* intensity measurements alone are insufficient to reconstruct them, as verified by the Gerschberg-Saxton simulations. This is due to the fact that the relationship between intensity, phase and amplitude is non-linear:

$$\mathrm{I} = \sqrt{A \, e^{-i\phi} * A e^{i\phi}}$$

Thus, these are not linearly-independent variables. Our simulations show that the solutions for $A, \phi(I)$ converge for large numbers of modes only with *4N* intensity measurements (see Fig 4). Note that this does not require 4 physical lanterns. This is because the lantern transfer matrices are only effectively coherent over a relatively narrow bandpass $\Delta\lambda_c$. Previous experiments have shown that an upper limit on this bandpass is

$$\Delta\lambda_c < \frac{\lambda^2}{D_{PL}}$$

while a lower limit is

$$\Delta\lambda_c > \frac{\lambda^3}{2\pi^2 \, \mathrm{N}A^2 \, D_{PL}^2}$$

For parameters similar to those we consider here, these correspond to bandpasses of ~30nm and ~6nm, respectively. As long as the source function is quasi-steady over this bandpass differences, we can then use multiple such bandpasses as independent intensity measurements for the phase and amplitude reconstruction. Importantly, this approach could allow us to reduce the number of physical lanterns (i.e. to one lantern) or reduce the port count of the dual lantern approach.

In the following sections V and VII, we describe our progress on establishing an experimental setup that will allow us to directly measure the decoherence bandpass of a photonic lantern. This will be a crucial parameter for finalizing (and simplifying) the PQI2 design.
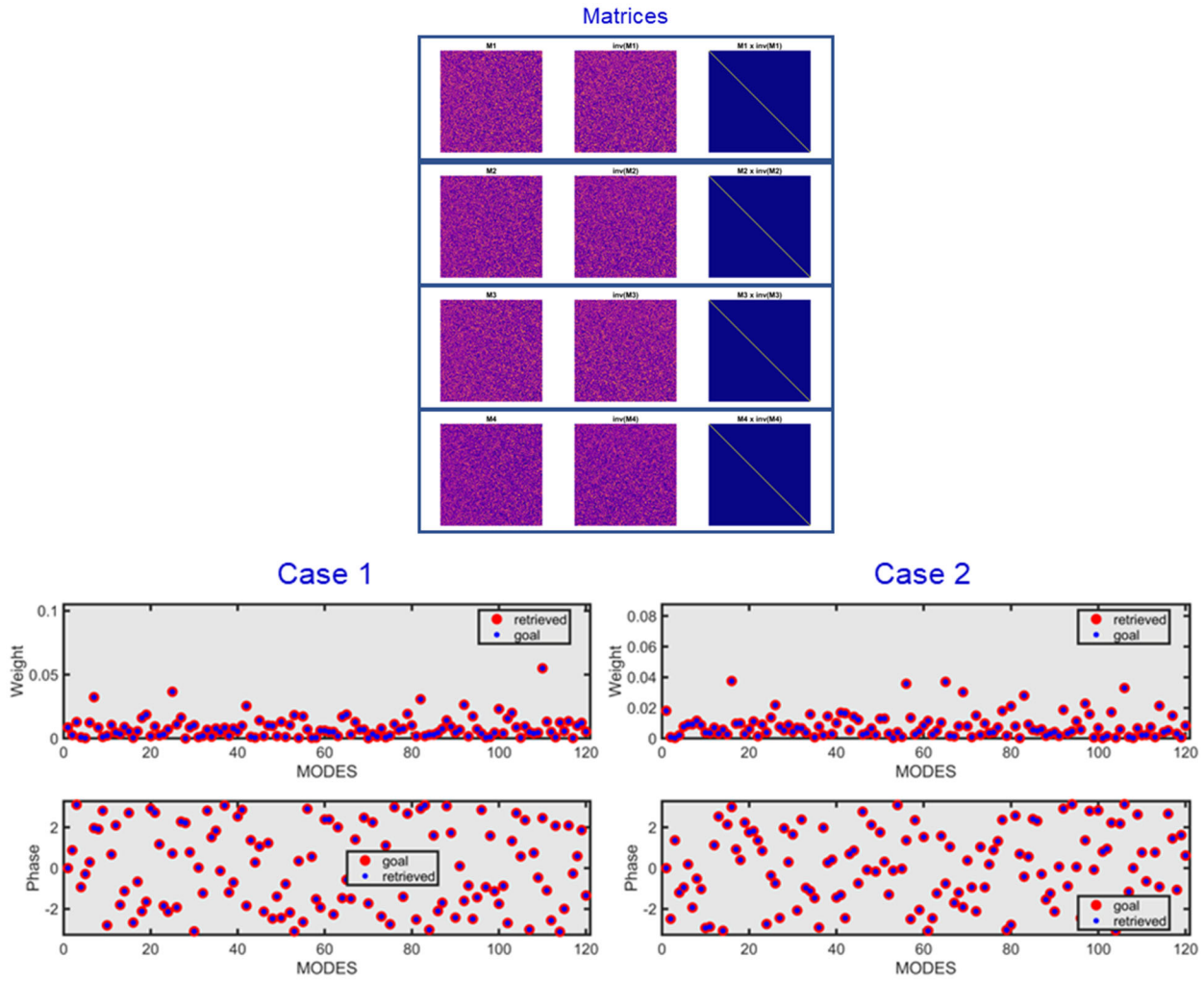
Fig 4 *– (Top) Example 4x 120-port matrices, with their inverses and resulting diagonal matrices (demonstrating their unitary nature). (Bottom) Reconstructed input vectors (weight = amplitude, and phase) for two different cases, demonstrating the high fidelity of the reconstructions compared to the initial input.*

B. Turbulence Phase Retrieval

Using the simulation framework above, we were able to confirm high-quality phase retrieval across a broad wavelength regime for source functions ranging from point-like to complex sub-DL sources by applying the wavelength diversity approach we outlined earlier. We show examples in Fig 5. In addition, we found that this approach continues to work even for slightly-resolved sources (~1.5 λ/D), and we are exploring potential applications for extended-scene wavefront sensing with PQI2-style systems. In addition, we confirmed that full turbulent wavefront information can be retrieved using a 200-mode (or higher) PL, consistent with the needs for source reconstruction (see next subsection) – see Fig 6.
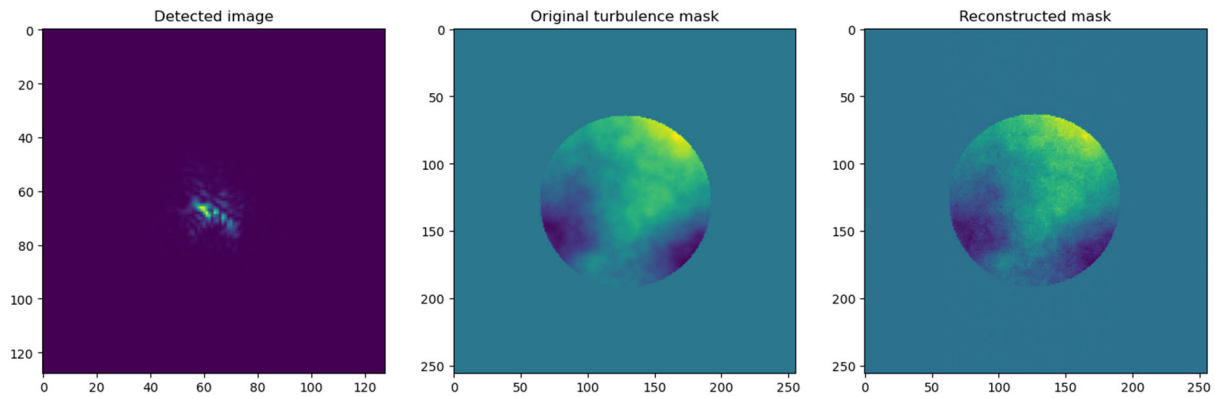
Fig 5 *– (Left) Turbulent image field. (Right) Original versus reconstructed phase map from two simulated wavelengths (550nm and 605nm).*
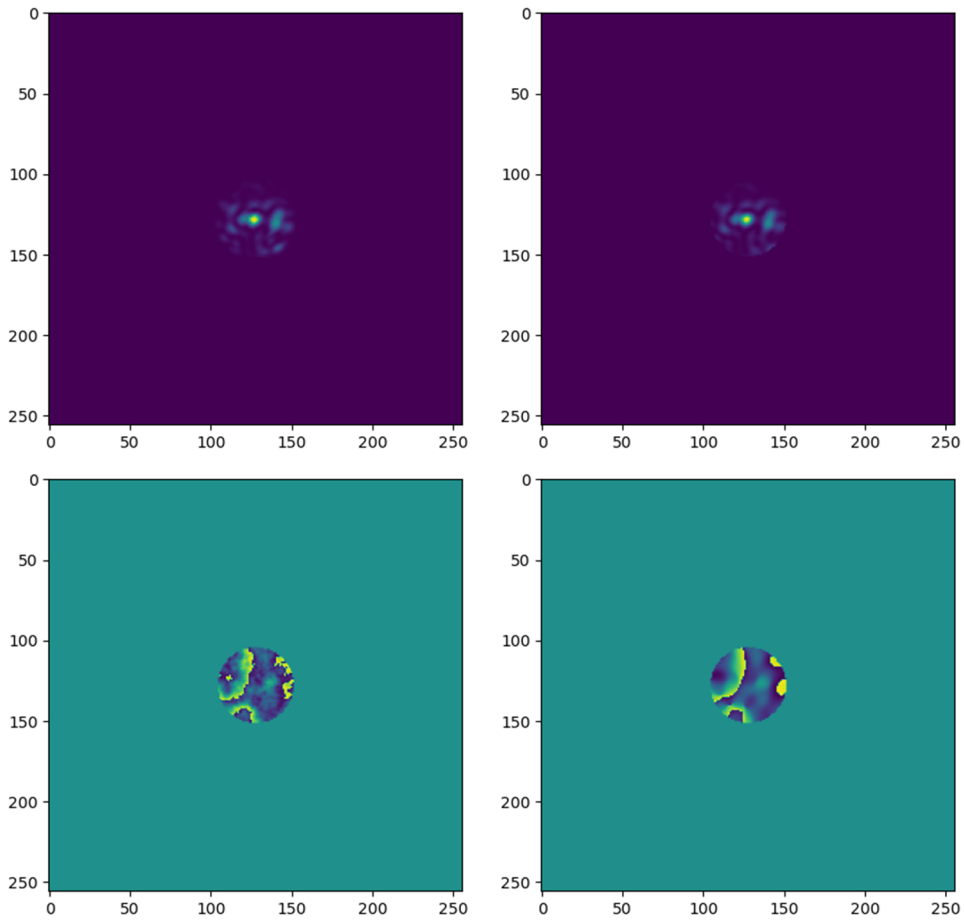

Fig 6 *– (Top left) Simulated turbulent PSF at 750nm for a 30cm telescope with r_0 = 3.7cm (550nm reference). These are the conditions expected in Orlando. (Top right) Reconstructed PSF from a 200-mode photonic lantern. (Bottom left) Phase map retrieved from the original PSF. (Bottom right) Phase map retrieved from the PL-reconstructed PSF.*

We combined all of these pieces to carry out end-to-end simulations of observations with PQI2 of various simulated target fields. These are all done at an instantaneous slice in time. The turbulence reconstruction is necessarily over a wavelength span (we simulate 600-1000nm), while the source function reconstruction is done at individual wavelength channels, allowing us to reconstruct a source spectrum. A primary focus of our effort in these simulations was to explore the limits of source construction imposed by the PL mode count. To evaluate this for the planned demonstrator observations, we assume a telescope diameter of 30cm, with r0 = 3.7cm (referenced to a wavelength of 550nm), an observing bandpass of 600-1000nm, with a reconstruction of the source function at λ = 750nm, and a spectrograph resolution of $R = \frac{\lambda}{\Delta\lambda} = 150$. We assume individual frame times of 5 milliseconds. The input source function has a separation of $0.25\frac{\lambda}{D}$ along the vertical image axis, with the lower source 5x brighter than the upper (centered source).

Using these parameters, we find excellent performance at $N_{modes} = 500 - 1000$, which is the parameter space we originally discussed in the Grand Challenge proposal. However, reducing the mode count is of interest as that relaxes the constraints on source brightness imposed by diluting the photon count per mode, as well as simplifying both PL and spectrograph design/fabrication constraints. Interestingly, we find that performance remains high for $N_{modes} = 300$ and that we can still recover sub-diffraction-limit source function separations at $N_{modes} = 200$ (see Fig 7). Further reducing the mode count to $N_{modes} = 100$ however, degrades the performance such that we can no longer distinguish the sources at this $0.25\frac{\lambda}{D}$ sub-DL separation. This refines our preliminary analyses at the proposal stage, where we anticipated a need for $N_{modes} \sim 1000$, indicating that a substantial reduction in mode count may be feasible for sub-DL source reconstruction.

We note that while the simulation software allows the inclusion of shot noise and detector noise, we are currently setting these to zero. This allows us to more easily study the impact of the various system parameters on performance, which is our primary focus at this time. Furthermore, we expect the signal per wavelength channel and per mode to be >10 photons per exposure time on a 2-m telescope for realistic sub-diffraction space debris source functions, indicating that we will be shot noise limited in the individual frames. For phase retrieval, the expected signal-to-noise ratio (combining the spectrograph wavelength channels) will be ~100 per mode per exposure, allowing for a high-quality phase retrieval limited by these systematic effects. The signal-to-noise for source function reconstruction (~3-4 sigma per mode per spectral channel) will then reach ~100 per mode in each individual exposure using wavelength combination and will be further augmented to very high levels by combining these individual frames over the observation time (>10,000 frames in <120 seconds of observation). For the current ~30-cm demonstrator, we will be observing brighter targets (i.e. binary stars) so that we can also reach the photon-noise-limited regime here. As we discuss in Section VII below, we will fold the shot/detector noise in fully once we have results from the PL experiments that will determine the final configuration of the system, as well as the machine-learning-based multi-wavelength reinforcement of the source functions.

5.   PHOTONIC LANTERN LABORATORY TESTS

A.   Photonic Lantern Fabrication

We focus our initial tests in the laboratory on demonstrating full amplitude/phase recovery for the lantern modes based solely on wavelength-resolved intensities – the basis of the PQI2 approach. We selected 19-port lanterns for this experiment as a compromise between the desire for larger count demonstrations and ease of manufacture and analysis. We are also primarily interested in the 600-1000nm bandpass that can be easily measured with the low-cost silicon-based CMOS/CCD detectors which are planned for deployment in the PQI2 demonstrator.

We have fabricated two 19-port lanterns for initial tests. The first (shown in Fig 8) consists of 19x SM800 single-mode fiber ports with 5.6μm cores and NA=0.11 outputs, and a 24.5μm NA=0.11 multi-mode input. This is optimized for single-mode operation at 800nm wavelengths. The second lantern is visually identical to the one shown in Fig 8, but consists of 19x SM600 fiber ports with 4.2μm cores and NA=0.11 outputs, and a 18.5μm NA=0.11 multi-mode input.
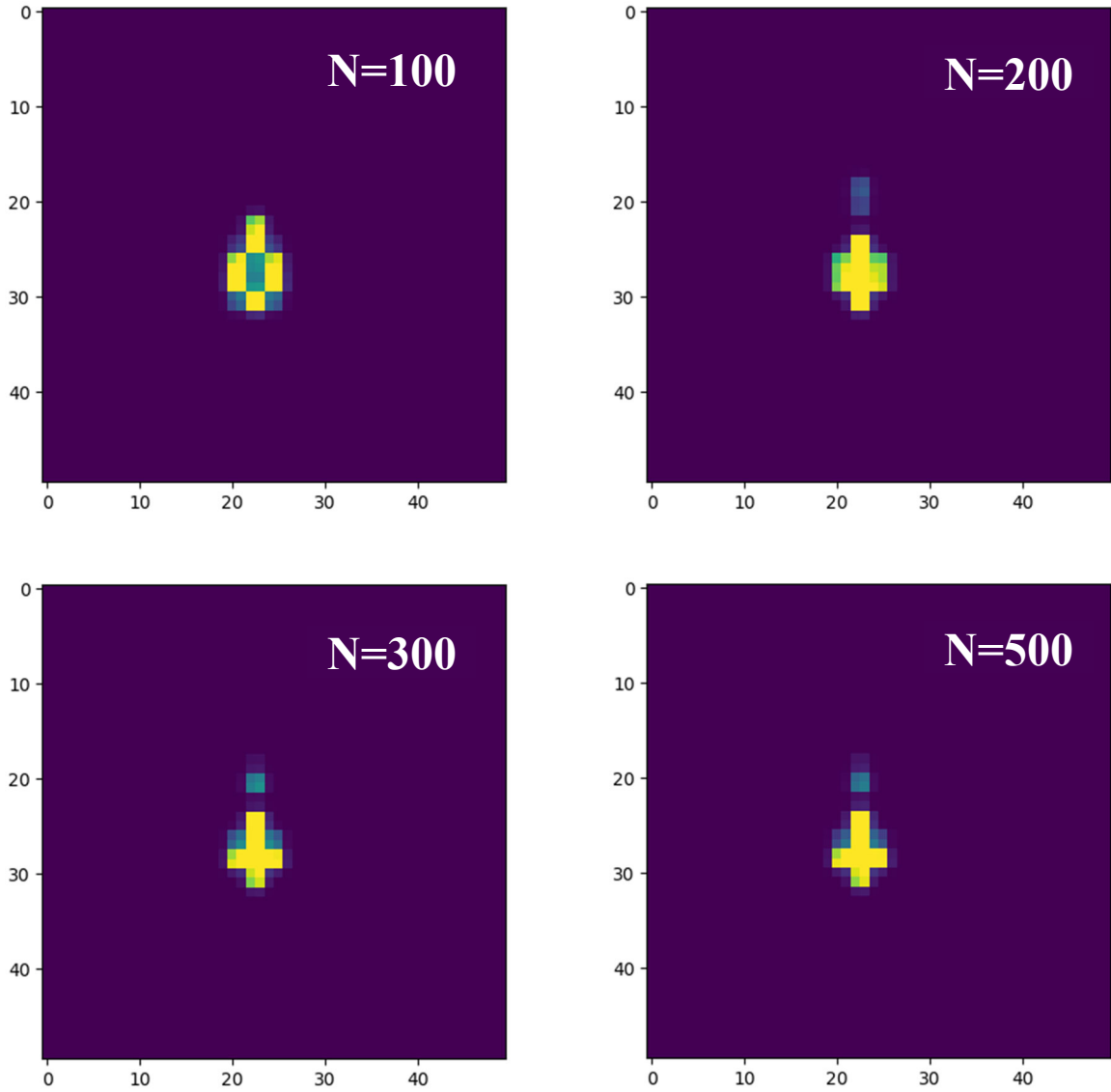
Fig 7 – Source function reconstruction versus mode count. *All have the same source function – 2 sources separated by 0.25 λ/D, with the top source 5x fainter than the bottom source. (Top Left) N=100 fails to distinguish the two separate sources. (Top Right) N=200 successfully distinguishes the two separate sources. (Bottom Left) N=300 clearly distinguishes the two separate sources, with compact source distributions for both. (Bottom Right) N=500 closely resembles the N=300 results, with some improvement in source compactness.*
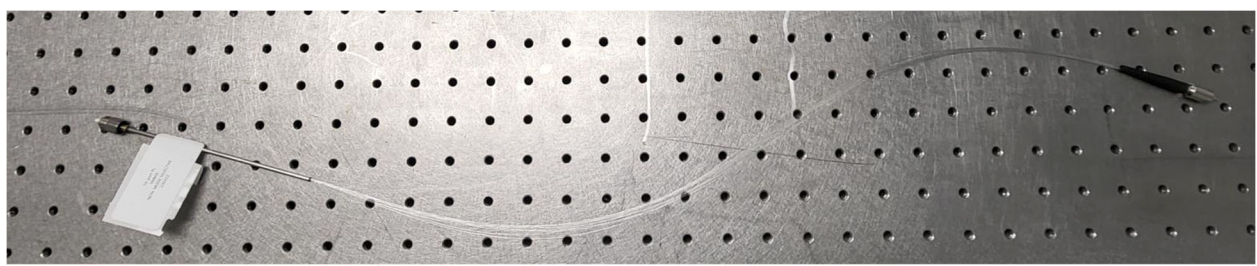
Fig 8 *– Fabricated 19-port photonic lantern with SM800 fiber ports. The multimode input is on the left end. The 19 output ports are bundled together in a single FC/PC connector on the right.*

B. Transfer Matrix Calibration

The most complete information about a wavefront is provided by its full complex distribution. By knowing the amplitude and phase distribution of the wavefront at one specific plane, it is possible to determine the characteristics at any other plane using Fresnel propagation.

Off-axis holography is an interferometric technique employed to analyze a signal wavefront, where both amplitude and phase information are retrieved. In order to use this technique, the interference pattern between the signal and a reference wave is recorded by an intensity detector in an off-axis geometry (hologram) (Fig. 10a). The intensity can be written as:

$$I = |E_R + E_S|^2 = |E_R|^2 + |E_S|^2 + E_R^* E_S + E_R E_S^*$$

where the first two elements $|E_R|^2 + |E_S|^2$ are known as the autocorrelation term, and do not provide any useful information. However, the last two elements $E_R^* E_S$ and $E_R E_S^*$, known as the real and twin images, encode the complex composition of the signal wave. Using numerical analysis, it is possible to retrieve simultaneously the phase and intensity information of the signal wave. Initially, a Fourier transformation of the hologram reveals the three aforementioned components (autocorrelation, real and twin images) (Fig. 9b). In the spatial frequency domain, the real image is filtered out from the two other components. Finally, a second Fourier transformation delivers the complex composition of the signal wave (Fig. 9c).
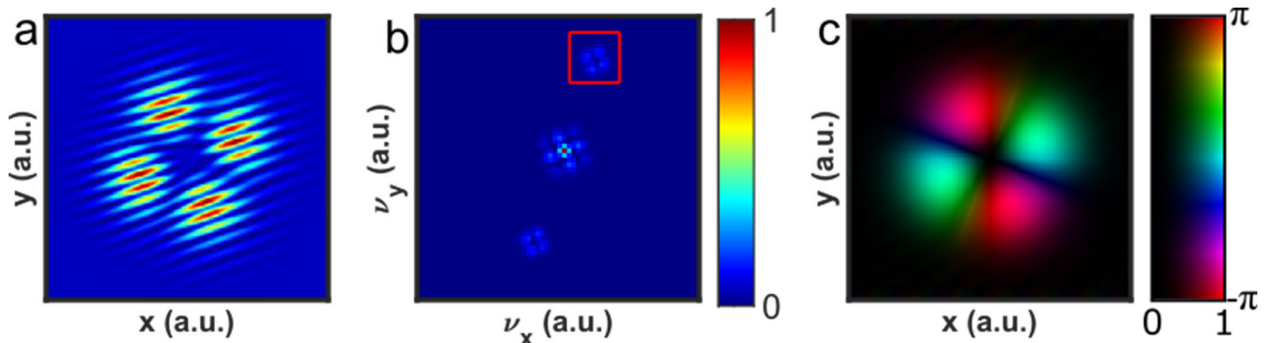

***Fig 9** - Holographic reconstruction of the complex properties of the synthesized field. **a**, The experimental interference pattern between the reference and the signal waves is recorded with a CCD camera in an off-axis configuration. **b**, The captured hologram encodes both phase and amplitude information of the signal wave. The complex composition of the signal can be retrieved by applying a filtering process in the spatial frequency domain of the initial hologram. **c**, Finally, the complex signal field is reconstructed by returning to the spatial domain.*

To implement the off-axis holography technique, a pump beam is split in two arms, one arm is used like the reference arm while the other arm (signal) is used to excite the photonic lantern terminals. The path length difference between reference and signal arms needs to be shorter than the coherence length of the pump beam. Finally, the interference pattern between reference wave and signal waves is recorded employing a CCD camera (Fig 10).

Once all the terminals of the photonic lantern are excited and the output field is analyzed, it is possible to construct the transfer matrix associated. Such a matrix fully encodes the properties of the photonic lantern device. We show the digital holography measurement system we fabricated for this work in Fig 11. In Fig 12, we show the transfer matrix image vectors measured at 850nm for the 19-port lantern shown in Fig 8.

We also find that the measured transfer matrices are largely independent of each other, as expected for these relatively large wavelength separations in these lanterns (see equation above) (Fig 13).
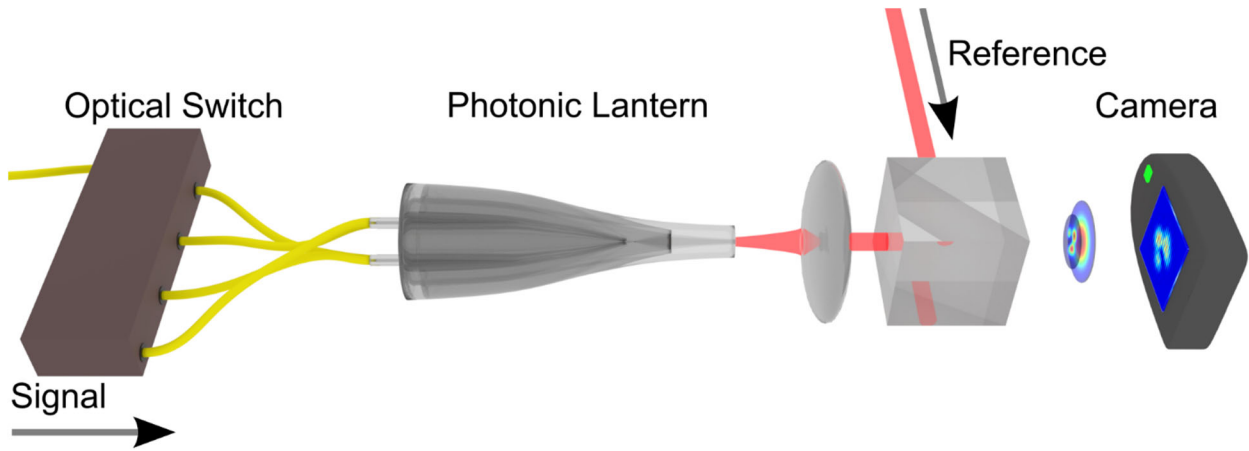
Fig 10 - *Schematic of the experimental setup to analyze a photonic lantern by off-axis holography technique. The pump beam is split in a signal arm and reference arm. The signal arm is used to excite the photonic lantern terminals. The interference pattern is recorded with a CCD camera.*
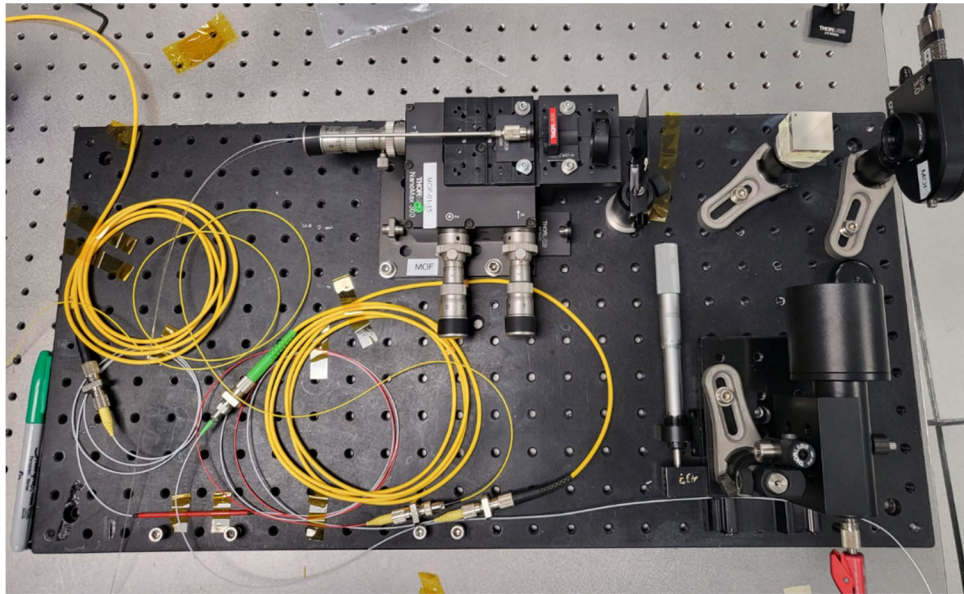

Fig 11 *– Digital holography testbed for photonic lanterns. A test lantern is installed in the system (center top, on the translation stages).*
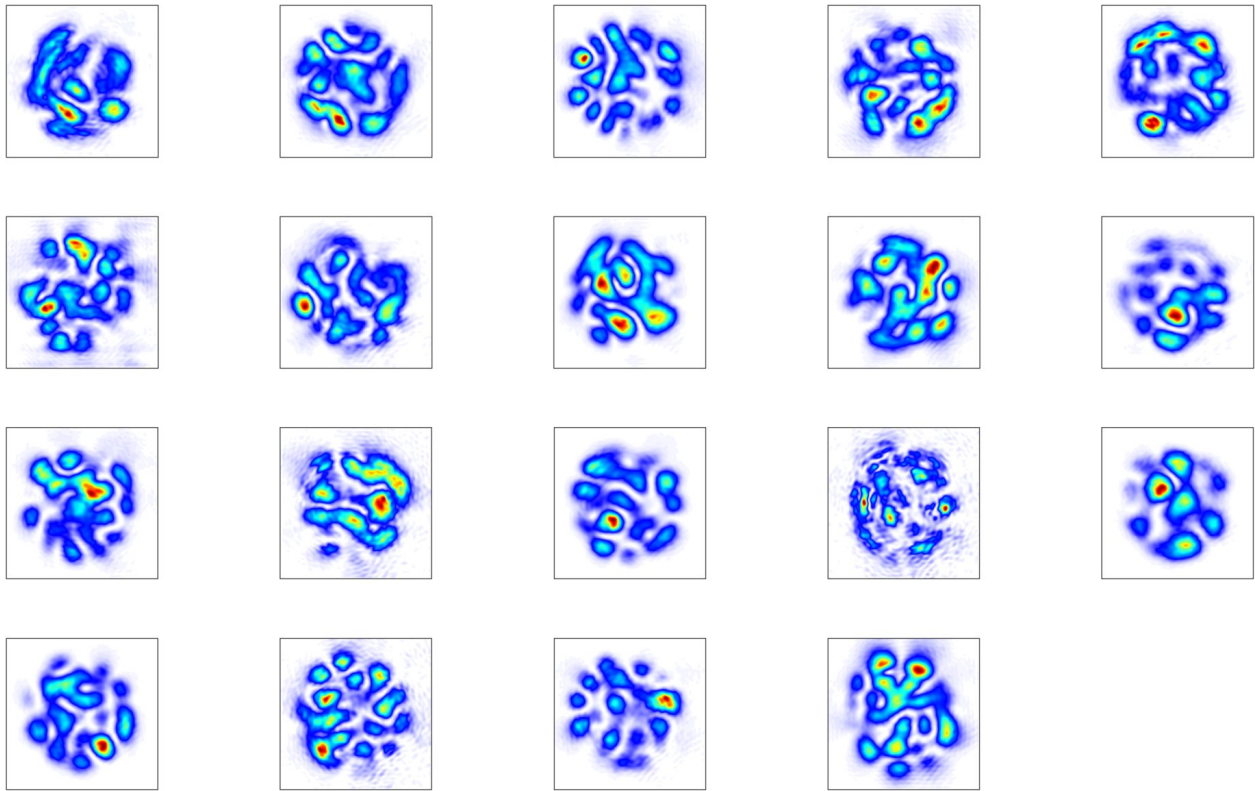
Fig 12 *– The 19 image intensity fields created at the PL multi-mode end by exciting each of the individual 19 single-mode ports one at a time.*
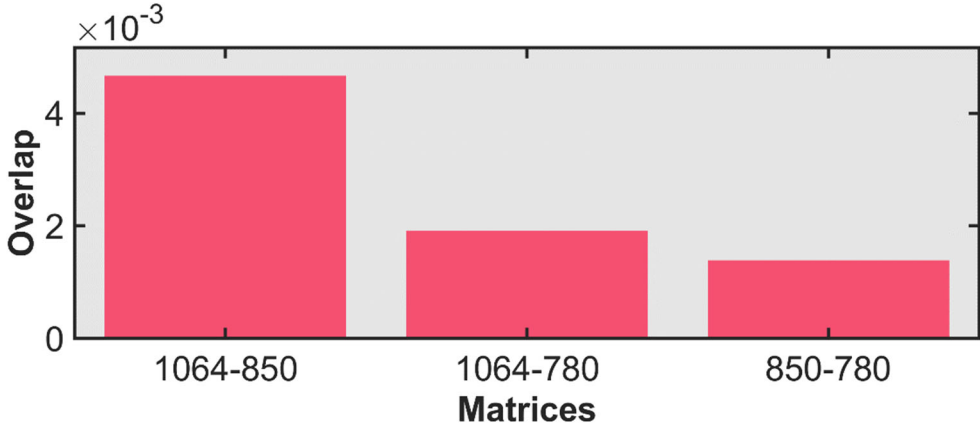

Fig 13 *– Overlap integrals for the measured transfer matrices at 780nm, 850nm, and 1064nm. All inner products are <0.005, indicating nearly-complete decoherence Our theoretical prediction for PL850 is a decoherence bandwidth of ~40nm, consistent with the experimental result*

C. PL Phase Reconstruction Tests

As noted above, after calibrating the transfer matrices of the lanterns using digital holography at discrete wavelength, we will then evaluate their behavior in a PQI2-style system. We have fabricated a testbed shown in Fig 14. We also show a hydrogen and helium arc lamp calibration spectra in Fig 15, as well as example phase masks and resulting images from the SLM system (Fig 16).
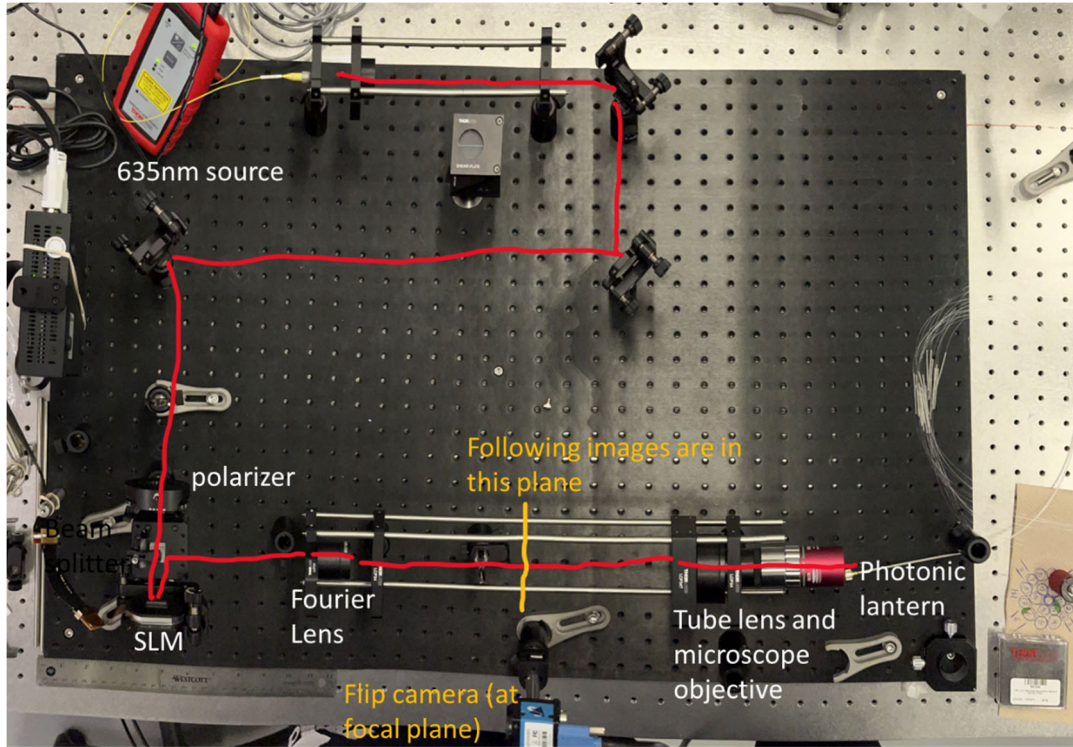

Fig 14 – *Photonic lantern testbed fabricated for this project. The light source (top center of the black bench) injects light into a series of fold mirrors and collimating/re-imaging optics, including a Spatial Light Modulator (SLM) (bottom left corner of the black bench). The light is then demagnified through a reverse microscope and injected into the multimode input of the photonic lantern (to be located on the translation stages at bottom right. Currently using a single-mode fiber for testing). The output end of the lantern is coupled to a spectrograph (silver bench at the bottom right), including a Nikon collimator, dispersing prism, Canon camera lens, and a red-bodied CMOS detector.*
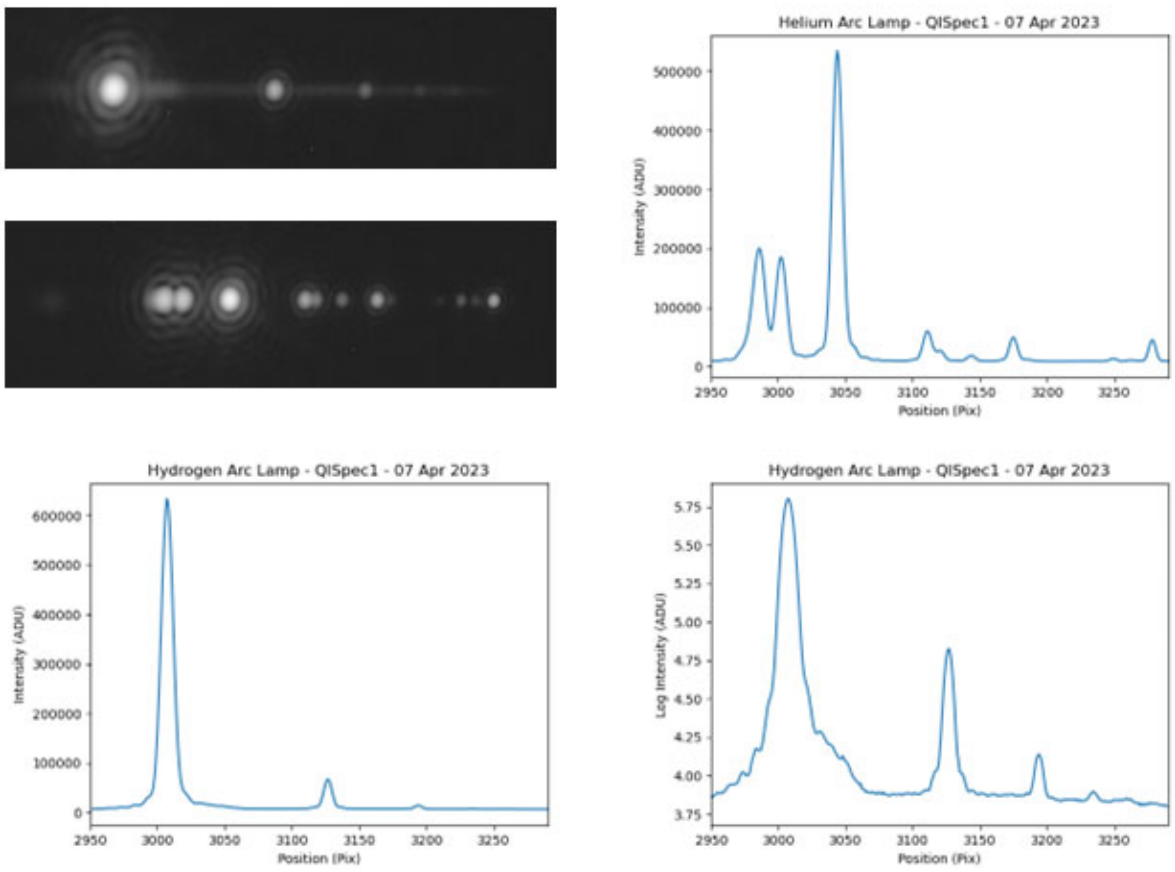
Fig 15 *– Laboratory test spectra. (Top Left) Hydrogen arc lamp spectrogram. Note clear Airy pattern on bright lines, indicating excellent diffraction-limited image quality. (Top Left, second row) Helium arc lamp spectrogram. (Top right) Helium lamp spectrum. Note multiple lines visible. (Bottom Left) Hydrogen arc lamp spectrum, linear scale. (Bottom Right) Hydrogen arc lamp spectrum, log scale. Note that the Balmer series lines Hα, Hβ, Hγ, and Hδ are all easily visible.*
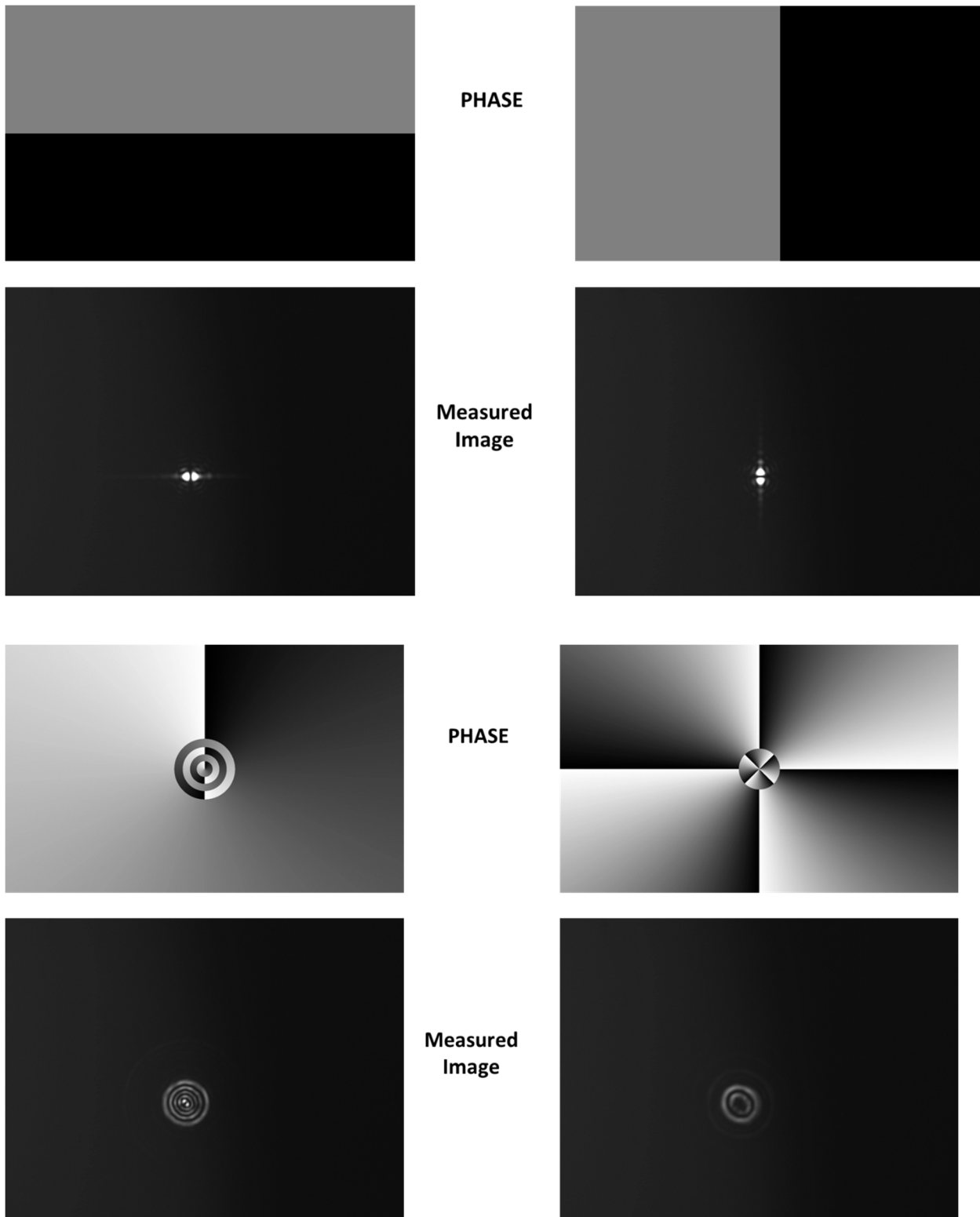
Fig 16 – *Programmed SLM Phase masks and resulting measured images. These used a 632nm laser for illumination. Top are HG modes 10 and 01, Bottom are modes LP14 and LP41.*

6. NEXT STEPS

The UCF/CREOL PQI2 concept was selected as the winner of the AFRL Grand Challenge in quantum-inspired imaging in late 2022, and this work began in 2023. As described above, we have carried out calibration of the 19-core photonic lanterns using the digital holography setup at 3 discrete (laser) wavelengths. We will then use the PQI2-style detector with the SLM input to characterize the decoherence bandpass of the lanterns. This will be the first such detailed measurement of any photonic lantern to our knowledge. It will provide key design drivers for the final simulations and design parameters of the photonic lantern. In addition, we have procured a laboratory atmospheric turbulence simulator. We will use this to characterize performance of a PQI2-style system on the laboratory benchtop. With the parameters provided above, we will run final transfer matrix simulations, including the observed decoherence versus wavelength of the lanterns, to better simulate the leverage provided by wavelength diversity in PQI2. We can then link the multi-wavelength solutions together in a realistic manner using machine learning, with the expectation that this will substantially improve the signal-to-noise and resolution achievable with PQI2 compared to the current (already-promising) results. The final simulations will also have shot/detector noise turned "on" for final assessments of expected performance. With the final simulation results and 19-core lantern tests, we will also determine the final design parameters for the PQI2 field demonstrator system. A key parameter will be the lantern mode/port count needed to achieve sub-DL source function reconstruction on-sky. This will have flowdown impacts on final design parameters for the rest of the system including telescope feed and spectrograph optics. With those parameters fixed, we will then proceed to the final mechanical design, including ready-for-fabrication drawings. We plan to achieve first light on-sky with a PQI2 system in Fall 2023.

REFERENCES

[1] M Matlin, E.F., Zipp, L.J. Imaging arbitrary incoherent source distributions with near quantum-limited resolution. Nature Sci Rep 12, 2810 (2022)

[2] Velázquez-Benítez, Amado M. ; Antonio-López, J. Enrique ; Alvarado-Zacarías, Juan C. ; Fontaine, Nicolas K. ; Ryf, Roland ; Chen, Haoshuo ; Hernández-Cordero, Juan; Sillard, Pierre ; Okonkwo, Chigo ; Leon-Saval, Sergio G. ; Amezcua-Correa, Rodrigo, Scaling photonic lanterns for space-division multiplexing. Nature Sci Rep 8, 8897 (2018).

[3] Moraitis, Christina D. ; Alvarado-Zacarias, Juan Carlos ; Amezcua-Correa, Rodrigo ; Jeram, Sarik ; Eikenberry, Stephen S., 2021, Applied Optics – Astrophotonics Special Issue, v60, i19, p. D93

[4] Leon-Saval,S.G., T. A. Birks, J. Bland-Hawthorn, and M. Englund, in Optical Fiber Communication Conference, Anaheim, California (2005), paper PDP25

[5] Bland-Hawthorn, Joss ; Leon-Saval, Sergio G., 2017, Optics Express, 25, 13

[6] Leon-Saval, Sergio G. ; Argyros, Alexander ; Bland-Hawthorn, Joss , 2013, Nanophotonics, 2, 429

[7] Birks,T.A., I. Gris-Sánchez, S. Yerolatsitis, S. G. Leon-Saval, and R. R. Thomson, 2015, Adv. Opt. Phot., 7, 2, 107